Neurocomputing 238 (2017) 365–376

Contents lists available at ScienceDirect

Neurocomputing

journal homepage: www.elsevier.com/locate/neucom

Dehazing for images with large sky region

Wencheng Wang[a,b,*], Xiaohui Yuan[b], Xiaojin Wu[a], Yunlong Liu[a]

[a] College of Information and Control Engineering, Weifang University, No. 5147 Dongfeng Street, Weifang, Shandong 261061, China
[b] Department of Computer Science and Engineering, University of North Texas, Denton, TX 76207, USA

ARTICLE INFO

Article history:
Received 16 July 2016
Revised 26 January 2017
Accepted 27 January 2017
Available online 7 February 2017

Communicated by Gaofeng MENG

Keywords:
Image dehazing
Quad-tree decomposition
Region growing
Transmission map

ABSTRACT

This paper introduces a haze removal algorithm based on region decomposition and features fusion to overcome the challenges of the dark channel prior-based algorithm, such as block effect and color distortion. In our proposed method, an image is decomposed with the quad-tree method based on gradient and grayscale information to obtain the sky regions. These sky regions are used as the seed point for region-growing, which will segment the image into sky and non-sky regions. A Gaussian filter is applied for smoothing on the segmented image, which is then used as a weight map to optimize the transmission image in the dark channel prior algorithm. Finally, the haze-free images are obtained based on an atmospheric scattering model and color compensation. Our experimental results demonstrated that images restored using this algorithm are generally clear and natural, and the algorithm is especially suitable for hazy images with large sky regions.

© 2017 Elsevier B.V. All rights reserved.

1. Introduction

In hazy scenes, the scattering of atmospheric particles degrades the images captured by optical sensors. Image contrast and color fidelity are affected to various extents, which directly impact human visual perception of the images as well as performance of computer vision systems. Thus, studies on image dehazing methods have great significance [1–3]. At present, processing methods for hazy images mainly include image enhancement-based approaches and image restoration-based approaches [4]. In image enhancement-based methods, the image visual effects are improved by contrast enhancement technique. The main techniques used are histogram equalization [5], Retinex [6], homomorphic filtering [7], and wavelet transform [8]. These techniques enhance the visual effects rather than actually dehaze the image. In image restoration-based methods, a hazy image degradation model is constructed based on the physical process of hazy image degradation. Lost information in hazy images is compensated using inverse operations. With strong pertinence, these methods can obtain natural dehazing effects, so they have received wide attention [9]. For example, Narasimhan and Nayar [10] obtained rough depth information by manually assigning the maximum and the minimum of depth of field, and then restored clear images based on physical model. Hautiere et al. [11] used an onboard optical sensor system to calculate scene depths and used 3D geographical models to perform dehazing. Kopf et al. [12] used existing geo-referenced digital terrain to reconstruct the 3D scene based on the known depth and textural information, and then performed model-based dehazing. This kind of method is based on the precondition that the depth of the scene is known, which severely limits the application of this algorithm in real-time system. In addition, Schechener et al. utilized the polarization property of atmospheric light [13] by taking a few pictures of the same scene at different polarization angles, and then restored the images by estimating the depth information based on the degree of polarization. While Nayar and Narasimhan [14] found another way to get the depth information of scene by capturing two images of the same scene under different weather conditions, through which the three dimensional structure is obtained to restore the clear image. Both of these two restoration methods require multiple images for processing. However, it is hard to obtain multiple images of the same scene under different conditions, which makes these methods difficult in practice.

Over the past few years, some single-image dehazing methods based on additional priors or constraints are proposed. For example, Tan [15] proposed an image dehazing approach by restoring the image contrast to its maximum extent based on the priori knowledge that haze-free images have higher contrast than the hazy images. However, this algorithm can easily lead to oversaturation. Fattal [16] used independent component analysis (ICA) and Markov random field (MRF) model to estimate the surface albedo based on the prior knowledge that there is no correlation between the object surface shading and transmission map, then

* Correspondence author at: College of Information and Control Engineering, Weifang University, No. 5147 Dongfeng Street, Weifang, Shandong 261061, China.
E-mail addresses: wwcwfu@126.com (W. Wang), xiaohui.yuan@unt.edu (X. Yuan), wfuwxj@163.com (X. Wu), fhylren@163.com (Y. Liu).

http://dx.doi.org/10.1016/j.neucom.2017.01.075
0925-2312/© 2017 Elsevier B.V. All rights reserved.

got the transmission of scene and recovered the clear image from the foggy one. This approach can usually produce impressive results when the color information is enough, yet it may fail in the cases when the assumption is invalid. He et al. [17] proposed a dark channel prior (DCP) dehazing method based on the statistical patterns obtained from haze-free image databases. This approach uses minimum filtering to estimate the medium transmission map and performs optimization to achieve good dehazing effects. Tarel and Hautiere [18] used median filtering to estimate the atmospheric veil function and then used a color tone mapping approach to obtain dehazed images. The restored images were clear and distinct, but halo effect may easily occur in areas that have rapid changes in depth of field. Kratz and Nishino [19] assumed that hazy images consist of two independent layers, the scene albedo and the scene depth, and used the concept of factorial Markov random field (FMRF) for modeling, eventually obtaining accurate depth information. However, some pixels in the images processed by this method were over-saturated. Later, Kim et al. [20] proposed a cost function based on image contrast and the degree of information loss, which effectively avoids disturbance due to bright objects when estimating ambient light, and applied this method to video dehazing. Ancuti and Ancuti [21] first demonstrated the utility and effectiveness of a fusion-based technique to restore a single hazy image. Later, Ma et al. [22] present a novel defogging algorithm based on a fusion strategy to improve the visibility of sea fog images, and Wang and Fan [23] proposed a multi-scale depth fusion (MDP) scheme which obtains the depth map of the physical model using an inhomogeneous Laplacian–Markov random field.

Among the methods above, the single image dehazing method by He et al. [17] has been further studied by other researchers due to its simple principle and excellent effects. Many improvements were done to refine the coarse transmission map based on DCP, such as WLS edge-preserving smoothing [24], bilateral filtering [25], guided image filtering [26], adaptive Wiener Filter [27], median filter and gamma correction [28], Laplacian-based gamma correction [29], median DCP (MDCP) [30] and a fusion strategy [31] to optimize the transmission image. Chen et al. [32] proposed an approach based on Bi-Histogram modification that exploits the features of gamma correction and histogram equalization to flexibly adjust the haze thickness in the transmission map of DCP. However, because the sky region does not meet the assumption of dark channel prior, block effects or serious color distortion may occur in the restored images due to an underestimated transmission map, which affects the image visual effects [33]. Jiang et al. [34] proposed a tolerance-based method to recalculate the transmission map of the bright areas. However, the tolerance calculation requires parameter tuning for different images. If the tolerance is too small, distortion cannot be completely eliminated; if it is too large, it leads to restoration errors in non-bright areas and also reduces the dehazing capability of the algorithm. This paper introduces an improved dark channel prior-based dehazing algorithm. It uses the concept of sky recognition to segment the sky component and the non-sky component, and conducts different dehazing processing on each component to achieve good results while eliminating block effect and color distortion. Additionally, the common problem that dehazed images are generally darker than the real scene is overcome using a color remapping technique to enhance the image visual effects.

The remainder of this article is organized as follows. In Section 2, atmospheric scattering model is introduced. The algorithm of image dehazing based on sky segmentation and transmission map optimization is described in Section 3, in which the sky segmentation principle, the quad-tree based method for estimating atmospheric light, fusion principle of transmission map and the image restoration method are described in detail. In Section 4, some experimental results are presented to be compared with other methods. Finally, some conclusions are introduced in Section 5.

2. Related work

2.1. Atmospheric scattering model

According to atmospheric scattering theory, imaging model of hazy scene contains two components: one is the attenuation process of reflection light from object to camera; the other is the scattering of air-light reaching to the camera. So, the imaging mechanism in bad weather can be described as the light attenuation model and air-light imaging model, which is the theoretical basis of foggy image with the characteristics of blur and low contrast, and is the main basis for us to understand the degradation mechanism of foggy image and restoring the image from degradation. Therefore, the scattering model to describe hazy images is expressed as:

$$I(x) = J(x)t(x) + A(1 - t(x)) \tag{1}$$

where x is the coordinates, $I(x)$ is the hazy image, $J(x)$ is the haze-free image, A is the atmospheric light, and $t(x)$ is the transmission map.

In this model, there are three components that are unknown, which makes it an ill-conditioned problem. $J(x)$can only be restored from $I(x)$ by estimating parameters $A$and $t(x)$.

2.2. Dark channel prior

The dark channel prior is based on a prior statistical patterns of haze-free images [17]: in most non-sky local areas, there is at least one color channel that has very low intensity values that may approach zero for some pixels, which can be expressed by the following equation:

$$J^{dark}(x) = \min_{c\in\{r,g,b\}} \left(\min_{y\in\Omega(x)} (J^c(y)) \right) \to 0 \tag{2}$$

where $J^c$is a color channel of J, $\Omega(x)$is a small image patch surrounding x, and J^{dark} is the dark channel image.

To estimate the transmission map$t(x)$, the atmospheric light A is assumed to be known, and the transmission map $\tilde{t}(x)$ in the local area $\Omega(x)$ is unchanged, then:

$$\tilde{t}(x) = 1 - \omega \min_{c\in\{r,g,b\}} \left(\min_{y\in\Omega(x)} \left(\frac{I^c(y)}{A^c} \right) \right) \tag{3}$$

where $\omega(0 < \omega \leq)$ is a constant which serves to maintain some residual of haze to improve the depth perception.

Due to the block effect in transmission map, soft matting or guided filtering [17] have been adopted to obtain an optimized transmission map image$t(x)$.

According to the atmospheric scattering model, once the transmission map $t(x)$ and atmospheric light A have been solved, the scene depth can be restored using Eq. (1) as follows:

$$J(x) = \frac{I(x) - A}{t(x)} + A \tag{4}$$

where A is estimated by identifying the top 0.1% pixels having the highest brightness inJ^{dark}, and then selecting the maximum values of the corresponding pixels in the original images.

2.3. Existing problem of DCP

The algorithm proposed by He et al. was based on a dark channel prior, so it was not applicable to white region such as sky or

Fig. 1. Dehazing effects using a dark channel prior method. (For interpretation of the references to color in this figure, the reader is referred to the web version of this article.)

water surfaces. Usually, the dark channel $J^{dark}(x)$ in these regions is much greater than zero, i.e.:

$$t(x) = (\,1 - I^{dark}/A\,) \quad < \quad \left(\frac{1 - I^{dark}/A}{1 - J^{dark}/A}\right) \tag{5}$$

So, the transmission map obtained using the algorithms above to estimate bright regions is usually smaller than the real value.

Eq. (1) is equivalent to

$$J(x) = I(x) + \left(\frac{1}{t(x)} - 1\right)(I(x) - A) \tag{6}$$

It is shown in Eq. (3) that the value of $t(x)$ is always less than or equal to 1, the single image haze removal thus can be regarded as a type of spatially varying detail enhancement [33,38]. The detail layer is given as $(I(x) - A)$ and the amplification factor is $(\frac{1}{t(x)} - 1)$ which is spatially varying. Since the intensity of the sky is usually very similar to the atmospheric light A in a hazy image, it can be shown that

$$(\,I(x) - A\,) \quad \rightarrow \quad 0 \tag{7}$$

Suppose the x is a pixel in sky region, $|A - I(x)| \in (\,0,\,20\,)$ and $t(x) = 0.1$, then, $J(x)$ will vary in $(\,I(x),\,I(x) + 180\,)$ according to Eq. (6), which implied that noise could be amplified and/or halo artifacts could be produced due to the large amplification factors. Thus, the colors in the final restored image are seriously distorted. Fig. 1(a) shows the original image and Fig. 1(b) shows the image restored using the dark channel prior method, with the area marked by the red rectangle magnified. The magnified image shows block effects and serious color distortion in the sky area and the image is dark, which distorts the overall visual effects. Hence, it is necessary to design a dehazing method specifically for the image with large sky region.

3.. Dehazing method based on sky segmentation

To overcome those problems, a dehazing algorithm based on the dark channel prior is designed specifically for haze removal in images with large sky region. This algorithm remaps the transmission map based on the sky region segmentation and optimizes the brightness of the restored images to enhance visual effects. The atmospheric scattering model is adopted and the dehazing method contains three steps. (1) Sky region segmentation: a quad-tree decomposition is conducted on the original images to obtain hierarchical bounding blocks of the sky sub-region, which is then used as the seed point of region growing to segment the whole sky region. (2) Transmission map fusion: a blurring filter is applied to the boundaries of the segmented sky region and the resulting image is regarded as a weight distribution map to remap the transmission maps acquired by the DCP method. (3) Image restoration: after obtaining the atmospheric light A, image restoration and brightness adjustment are performed using the atmospheric scattering model. The overall process of the dehazing algorithm is shown in Fig. 2.

3.1. Sky region segmentation

For hazy images containing the sky, it can be observed that the colors of the foreground are relatively vivid, while the colors of sky areas are gray and homogeneous due to the haze. Thus, in order to discover smoothly connected areas with high brightness values and mark them as sky, a segmentation method based on region growing is adopted. The steps are described in details.

(1) Automatic seed point selection.

The basic principle of the region growing is to use a single pixel as the initial seed to incorporate similar pixels around the seeds into one region. Therefore, the selection of the seed point, i.e. the initial pixels, directly influences the results. To adaptively select the seed point, quad-tree decomposition method is used for searching. The basic process is to divide the image into four blocks of the same size firstly and estimate if each block meets specified conditions. If condition is satisfied, the image block is further divided into four sub-blocks using the same approach. This process is iterated until the termination condition is met. The decomposition structures are shown in Fig. 3.

To estimate the value of atmospheric light A, Kim et al. suggested choosing the region with the largest average intensity for further decomposition [20]. This method acquires sky sub-regions in most cases, but could fail when white objects are present in the image. Fig. 4 shows the image "LAKE". Due to disturbance caused by reflected light from the lake surface, the quad-tree decomposition, which takes the average gray value as the criterion, leads to a sky area positioning error, as shown in Fig. 4(b).

To improve the robustness of sky location, we assume that the sky area usually occupies the middle or upper part of the image, and multiply a coefficient which is less than 1 to the lower section of the image during decomposition, which is expressed as:

$$I(x,y) = \begin{cases} I_g(x,y) & 1 \le y \le M/2 \\ \eta\, I_g(x,y) & M/2 < y \le M \end{cases} \tag{8}$$

where η is the weight coefficient, less the η, more probability of the sky on the upper part of image will be.

Assuming that the image is evenly divided into four parts $x_n^i, i \in [1, 2, 3, 4]$ indicates the upper-left corner, the upper-right corner, the lower-left corner and the lower-right corner, respectively. n is the level of iterations, and in the initial decomposition, $n = 1$. The ratio of average grayscale and gradient value of each region $S(x_n^i)$ is defined as the score of this region x_n^i, the formula is expressed as:

$$S(x_n^i) = mean(x_n^i)/gradient(x_n^i) \tag{9}$$

where *mean* indicates the average gray scale value and *gradient* indicates the average gradient in this region.

For the above decomposition process, there is an absolute termination condition, i.e., for the nth level decomposition, if the difference between the maximum and the second maximum is less than S_T, then the decomposition terminates. Assume that for the nth iteration, the largest decomposition times are expressed as$S(x_n^k)$, the termination condition is:

$$\min \left| S(x_n^k) - S_n(x_n^{\bar{k}}) \right| \le S_T \tag{10}$$

where min is the minimization operation, and $\bar{k}$ indicates the areas excluding area k.

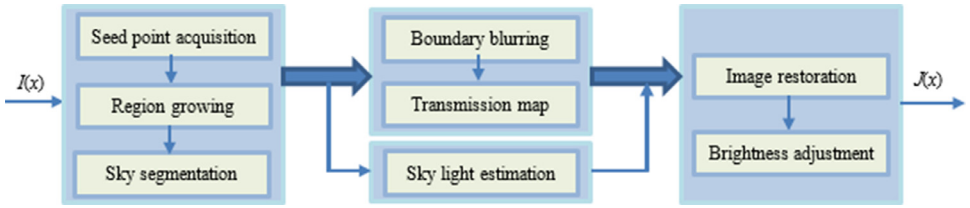

Fig. 2. Diagram of proposed algorithm.

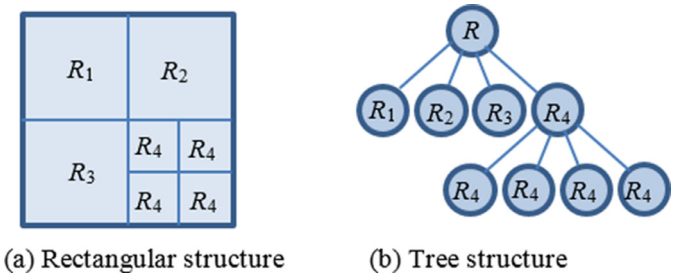

Fig. 3. Quad-tree decomposition types.

Fig. 5 is the decomposition results of different S_Ts, from which it can be seen that the termination of quad-tree decomposition will change faster when S_T is larger.

Using the above rules, the sky is obtained. Since this is the optimization of Kim's method [20], it more applicable for the images including water surface or white objects. Some results are shown in Fig. 6, where the first row includes original images, the second row includes the results with Kim method, and the last row includes the result of our method, which can be seen that our method got more accurate sky region.

In later steps, this area is used to extract seed point for segmentation. The rule for the region containing the seed points is defined as follows: set the size of the seed point area to $[m \times n]$. The gray value of any point (x, y) in $D$is denoted as$R(x, y)$, and the average gray scale value of D is calculated as:

$$R_{ave} = \frac{1}{mn} \sum_{(x,y)\in D} R(x, y) \tag{11}$$

Calculate the grayscale difference between every point in D and R_{ave}:

$$R_{dif}(x, y) = |R(x, y) - R_{ave}| \tag{12}$$

Select (x_s, y_s) as the seed point to make $I_{dif}(x_s, y_s) = \min_{(x,y)\in D} R_{dif}(x, y)$. Using this method, the acquired sky area and the seed point are shown in Fig. 7. Fig. 7(a) shows the results of the quad-tree decomposition using proposed method, where the red rectangle belongs to sky region, and Fig. 7(b) shows the seed point calculated using Eqs. (11) and (12).

(1) Criteria and process of the region growing method.

After seed point P has been selected, region growing starts from P, and search the eight neighborhoods around this point. A threshold T is specified, and when the difference between the search point's gray and that of point$P$is less than$T$, the point will be considered part of the same target and marked as L. The above process is repeated and the search continues outwards to adjoining neighborhoods until disqualifying pixels are found. The area corresponding to the target image is finally obtained.

The growing criteria to calculate the similarity between the pixels in the seed area and the pixels under examination (i.e., the 8-connected pixels and the pixels newly grown from the seed area) is shown below:

$$|I(x, y) - M| \le T \tag{13}$$

where $T = k\sigma$, M and σ indicate the grayscale mean value and standard deviation respectively for all pixels within the present grown area, and k is the customized coefficient, which is multiplied by σ to be used as the threshold for region growing. If the grayscale of a neighborhood pixel is within this range, then it is accepted; otherwise, it is rejected.

The flowchart of the region growing algorithm is shown in Fig. 8. Firstly, one or more points in the target areas (seed area) are selected and then added to the grown area. These points are then taken as the starting points and the new grayscale values, and standard deviations of all the pixels in the grown areas are calculated. Next, it is determined whether the neighborhoods of the present area have pixel points that meet the growth criteria. If they do, then these points are added to the grown area and the first iteration has been completed. After the first iteration, the above steps are repeated until no qualifying neighborhood pixel points can be found and the region growing algorithm terminates.

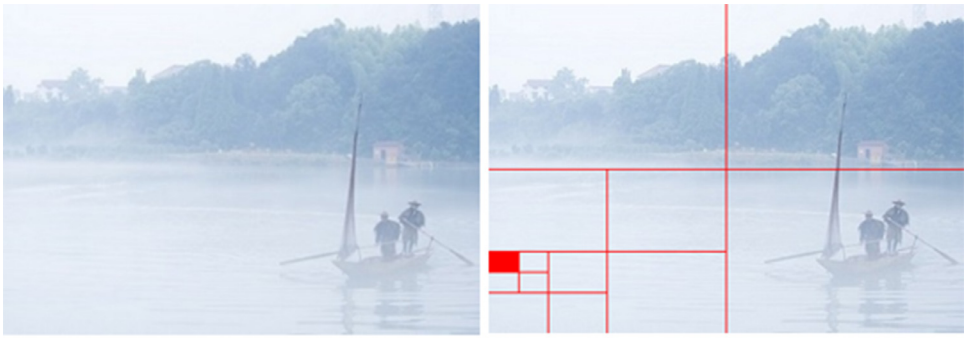

Fig. 4. Image decomposition results based on quad-tree [20].

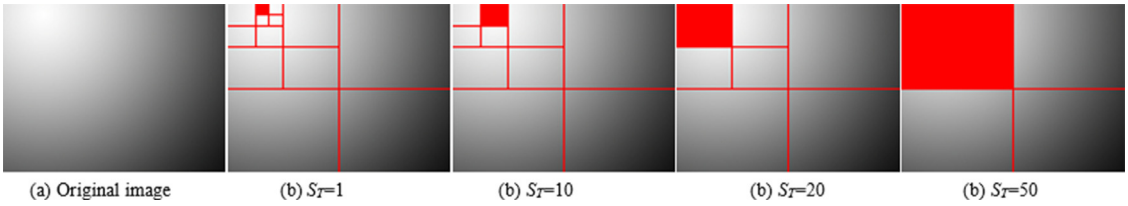

Fig. 5. Decomposition results of different S_T.

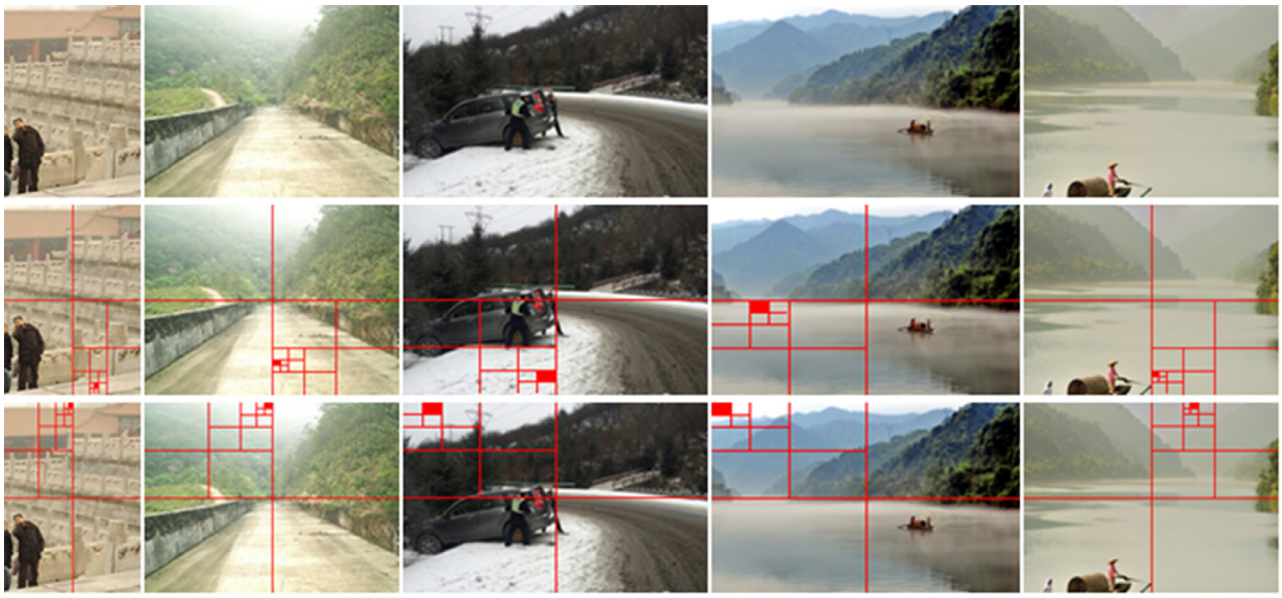

Fig. 6. Comparison of Kim method [20] and our method.

Fig. 7. Seed point acquisition. (For interpretation of the references to color in this figure, the reader is referred to the web version of this article.)

Finally, all the pixels in the overall image will be segmented into two types: sky region and non-sky region, which can be expressed as a binary image as follows:

$$g(x,y) = \begin{cases} 0 & Non-sky\ region \\ 1 & Sky\ region \end{cases} \quad (14)$$

A sky segmentation example is shown in Fig. 9, where Fig. 9(a) contains the hazy image including sky, and Fig. 9(b) shows the sky area in white and the non-sky area in black.

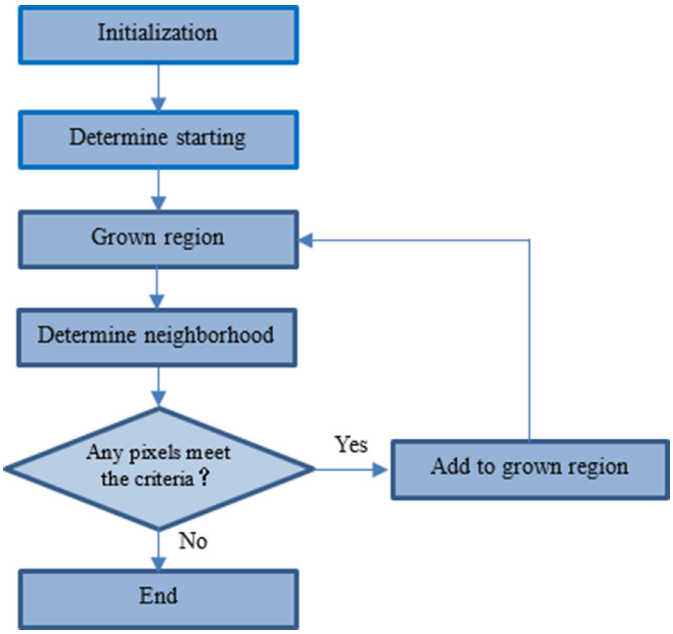

Fig. 8. Flowchart of region growing.

3.2. Atmospheric light estimation

Another key factor in solving the hazy imaging equation is the estimation of atmospheric light*A*. According to haze's characteristics, a heavy haze will increase the brightness of the target scenery. Therefore, Tan et al. took the maximum pixel value in thick haze areas of an image as the atmospheric light *A* [15]. In the method by He, the highest original pixel values of the top 0.1% brightest pixels in the dark channel priori images were regarded as atmospheric light *A* [17]. However, when there are white objects in a scene, if the window selection during the dark channel image acquisition is not appropriate, the white objects will not be eroded, which will

(a) Original image (b) Sky segmentation

Fig. 9. Sky region segmentation.

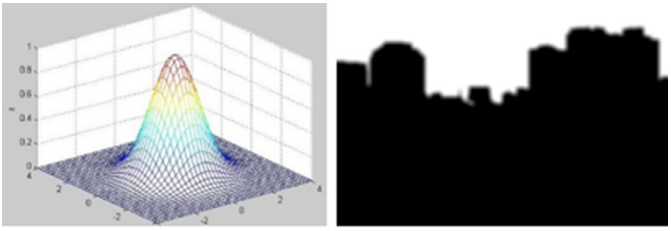

(a) Gaussian distribution (b) Image blurring

Fig. 10. Border blurring.

cause the selected atmospheric light intensity to be based on the white object. The atmospheric light values obtained by the above-mentioned two methods may be different from the actual value.

As discussed in Section 3.1, the atmospheric light value can also be obtained from the decomposed sky area image. First, the pixel values in the sky area are extracted. Then, the pixel values in this area are sorted in descending order. Finally, the average gray values of the top 1% pixels with the largest brightness values are selected as the atmospheric light value A, expressed as follows:

$$A = mean(\overset{0.01}{\max} R(x)) \tag{15}$$

The thickest hazy region obtained by the above methods is marked with 1. Experimental results have demonstrated that this approach can compensate for the impact of white clouds in sky areas to a certain extent, and also remove evaluation deviations caused by salt-and-pepper noise that may exist in images.

3.3. Transmission map fusion and refinement

After A is calculated, the principle of sky recognition and dark channel prior are combined, and Eq. (3) is used to estimate the transmission map $\tilde{t}(x)$. As the transmission map in the sky area is small and uneven, it is uniformly set as a constant value t_{sky}, while the non-sky area maintains the calculation of transmission map, that is:

$$t(x) = \begin{cases} t_{sky} & I_{seg}(x) = 1 \\ \tilde{t}(x) & I_{seg}(x) = 0 \end{cases} \tag{16}$$

However, since the transmission map in the sky area is set to be a constant, there will be a sudden change at the border between the sky regions and the non-sky regions. Therefore, in order to improve the visual effects, image fusion technology is required to fuse t_{sky} and $\tilde{t}(x)$ by a certain proportion. In this paper, a weighted average algorithm in data-level fusion is adopted to smooth the medium transmission map using the equation below:

$$t(x) = \omega_1 \times t_{sky} + \omega_2 \times \tilde{t}(x) \tag{17}$$

where ω_1 and ω_2 are the weight coefficients with the constraint condition$\omega_1 + \omega_2 = 1$.

Every point in the acquired binary image after sky area segmentation either belongs to the sky or not. However, after applying the blurring filter to the boundary area to smooth the transition, the result image can be regarded as a weighted image of $\tilde{t}(x)$, which is used for transmission map fusion. The Gaussian blur method is used to transform each pixel in the image into a weighted average of all pixels in the neighborhood, which has isotropy and uniformity features. For example, if the size of a 2D template is $m \times n$, then the Gaussian function corresponding to element (x, y) in the template is:

$$G(x, y) = \frac{1}{2\pi\sigma^2} e^{-\frac{(x-m/2)^2+(y-n/2)^2}{2\sigma^2}} \tag{18}$$

where σ is the standard deviation of the normal distribution.

By performing convolution between the non-zero blurring kernel matrix and the original image, a filtered distribution is obtained:

$$I'_{seg}(x) = I_{seg} * G \tag{19}$$

where $*$ denotes convolution. Each pixel is a weighted average of the neighboring pixels. The original pixels coincide with the mode of the Gaussian distribution, and have the largest weight. Neighboring pixels that are further from the original pixels have smaller weights. This blurring process is better at retaining the boundary than other isotropic blurring filters.

Finally, the transmission map fusion method is given below:

$$t(x) = t_{sky} I'_{seg}(x) + \tilde{t}(x)(1 - I'_{seg}(x)) \tag{20}$$

where the fixed transmission map value in the sky area is t_{sky}. When $I'_{seg}(x) = 1$, that is it definitely belongs to the sky, the transmission map becomes to a fixed value. When $I'_{seg}(x) = 0$, the normal dehazing is performed. Fig. 10(a) shows a Gaussian kernel diagram, Fig. 10(b) shows the processed results of Fig. 9(b), in which the bright areas and dark areas represent the sky area and the non-sky area, respectively.

Since rough transmission estimation can lead to block effects in the restored image, a guided filter is used to optimize the medium transmission map. This method assumes that there is a local linear relationship between the guiding image I and the filter output q, that is:

$$q_i = a_k I_i + b_k \qquad \forall i \in \omega_k \tag{21}$$

where ω_k is a template with radius r, a_k and b_k are the constant coefficients in the window, which makes the border of the output image$q$ and the guided image I be consistent in fulfilling the purpose of both maintaining semicircle information as well as smoothing the image. In this paper, the rough transmission map obtained using Eq. (18) is the input of the guided filter, the hazy image is the guided image, and thus the optimized transmission map will then be obtained. For example in Fig. 11, after processing the guided filter, the border characteristics of the output medium transmission rate are remarkably improved, and the connection between the border and the flat area is more natural.

Fig. 12 is the transmission map (the first row) and recovery (the second row) when t_{sky} changes. Seen from the graph, the color distortion of the output image becomes more serious as t_{sky} becomes larger. In the actual process, t_{sky} is usually set to 0.35 by experience.

3.4. Image restoration and tone adjustment

After the transmission map $t(x)$ and the atmospheric light A have been computed, the haze-free image of the scene under ideal conditions can be directly restored using Eq. (4). When $t(x)$approaches zero, the direct attenuation term also approaches zero, which increases the dehazed image pixel values by too much. At this time, the restored image may contain noise. So, a lower

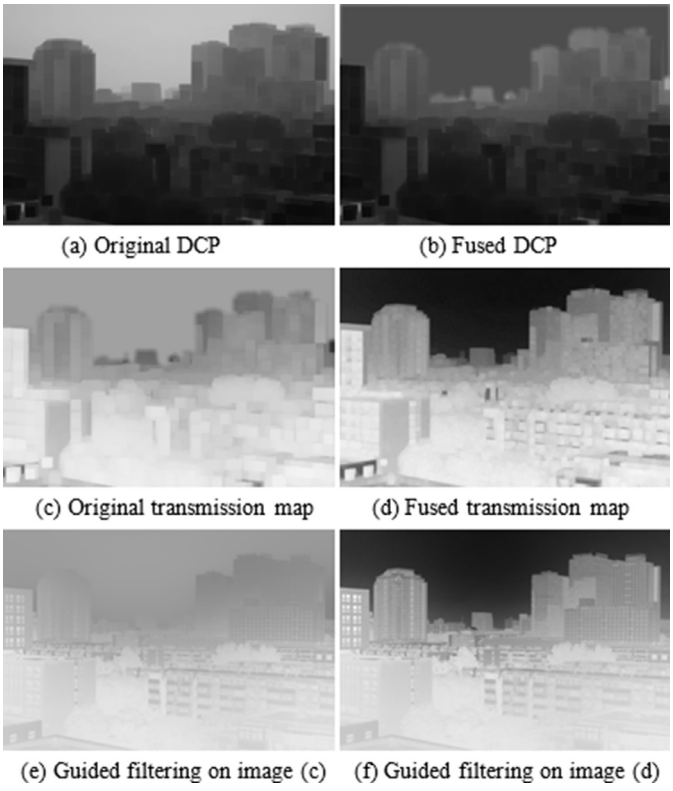

Fig. 11. Transmission map fusion.

bound $t_0$is set for the transmission map$t(x)$, which makes the dehazing effects more natural. The final dehazing image J is expressed as:

$$J(x) = \frac{I(x) - A}{\max(t(x), t_0)} + A \tag{22}$$

where $t_0$is the set constraint condition, which is set to 0.1 in this experiment.

In addition, since the image is affected by the surrounding environment and the lighting on hazy days, parts of the images may have low brightness and the restored images based on dark channel prior will be even darker. According to Weber–Fechner Law [35], the subjective brightness perceived by human eyes is acquired by nerve stimulation caused by reflected light of the object shining on the human eye's retina. The subjective brightnessL_d and the objective brightness L_0 present a logarithmic linear relationship, i.e., $L_d = \beta \log L_0 + \beta_0$where β and $\beta_0$are constants. The relationship between the subjective brightness and the objective brightness is shown in Fig. 13(a), and this curve is used to adjust the tone of the restored images. In order to avoid the increase of computation complexity led by the logarithm operation, in the actual application of this method, a simple function is adopted to match Fig. 13(a) with the obtained function expression as shown below:

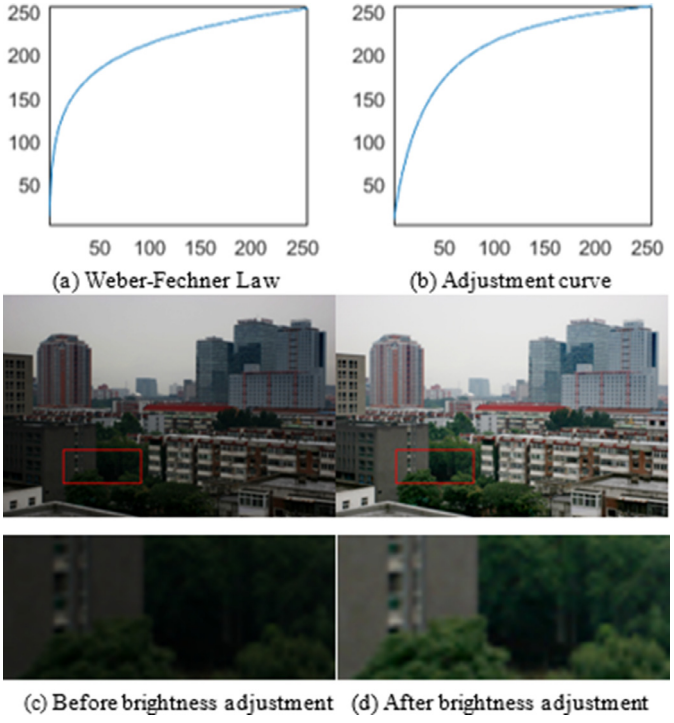

Fig. 13. Brightness adjustment.

$$L_d = \frac{L_0(255 + k)}{L_0 + k} \tag{23}$$

where k is the adjustment coefficient. As shown in Fig. 13(b), the smaller its value is, the larger the adjustment range should be, In the experiments, $k$is acquired based on the average value of the gray level image, and its value is calculated using $k = 1.5mean(I(x))$, where *mean* is the average value. An image comparison before and after the adjustment is shown in Fig. 13(c) and (d),

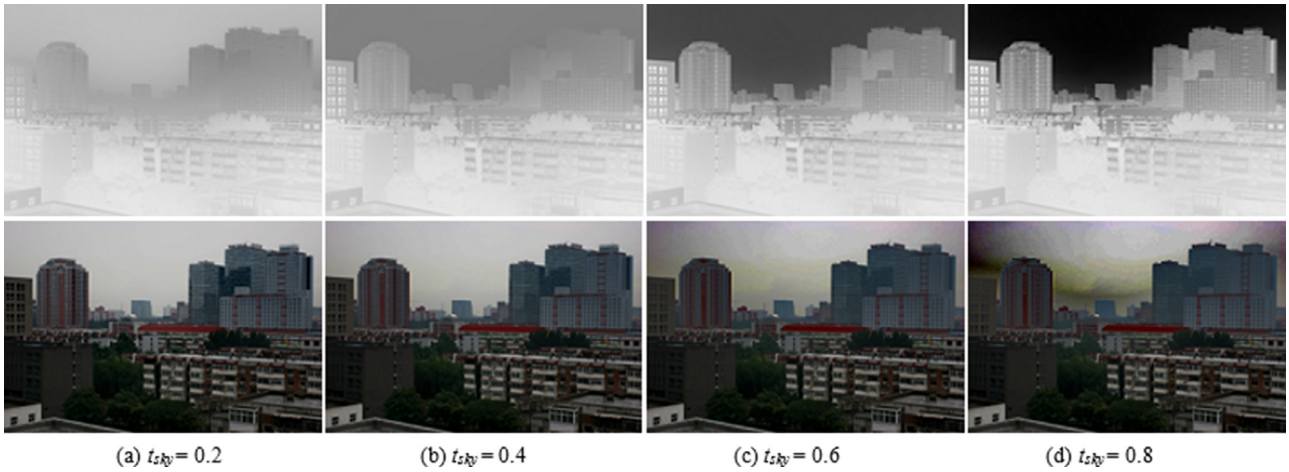

Fig. 12. The output of transmission map and recovery when t_{sky} changes.

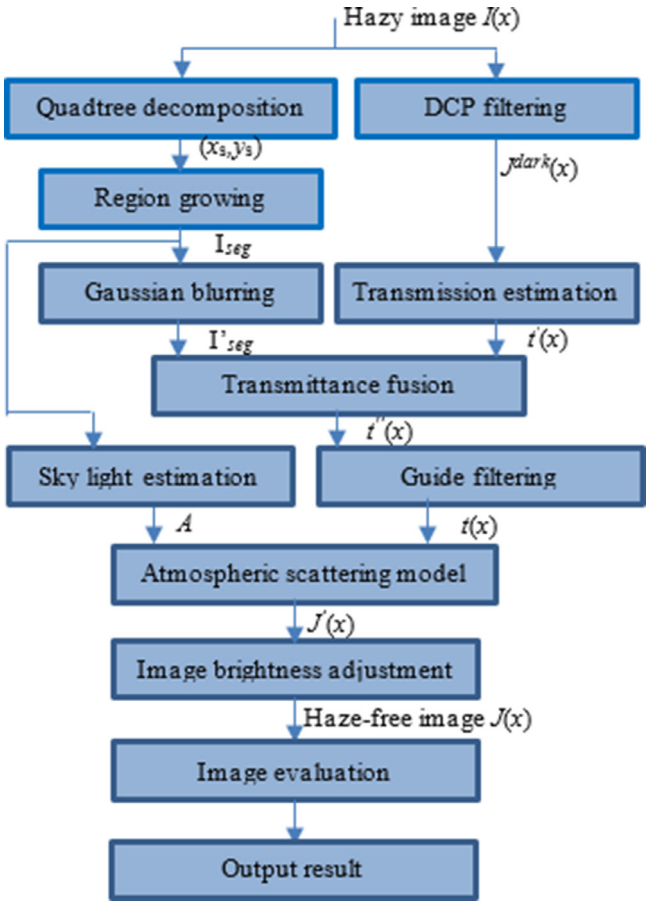

Fig. 14. Overall work flow of this algorithm.

where the lower images are the magnified areas of the rectangles. In Fig. 13(c), although the haze is removed, the overall brightness is poor – the image is dark with bad tone. Compared to Fig. 13(c), the overall brightness and contrast of the adjusted image in Fig. 13(d) have been improved, and the visual effects are closer to the real scene that would be seen under conditions on a fine day.

The flowchart of this algorithm is shown in Fig. 14.

4. Experimental results analysis

In order to analyze the effectiveness of the dehazing algorithm, an experimental platform is built and the program is written. The experimental hardware platform is a Dell laptop with Intel(R) i7-5500 U CPU@2.4 GHz and 8G RAM, and the testing software is Matlab 2014b running on Windows 8.

Fig. 15 shows the processed results of the experimental images using our method, where Fig. 15(a) is the original image; (b) is the sky search result, with the sub-area of the sky marked with a red rectangle; and (c) is the result of the sky segmentation, where the white region is the sky and the black region is non-sky. This demonstrates that this algorithm can accurately recognize sky region and non-sky region (almost consistent with the result that can be observed by human eyes). Fig. 15(d) is the transmission map after fusion; and (e) is the final restored image result. The final image shows clear details in the restored image with a natural transition between the sky area and the non-sky area, which demonstrates the feasibility and effectiveness of the transmission map estimation method proposed in this paper.

We compared our method with the classical enhancement-based methods [5–8], He's method [17], Tarel's method [18], Meng's method [36], and Zhu's method [37]. The comparison parameters include visual evaluation and computational complexity [39,40].

4.1. Visual evaluation

Fig. 16 shows a comparison of experimental results between the proposed method and some traditional enhancement-based methods. Fig. 16(a) is the hazy image. Fig. 16(b)–(h) are the images processed with histogram equalization, the Retinex method, the homomorphic filtering, the wavelet transform, and the proposed algorithm, respectively. As shown in Fig. 16(b)–(f), in the visual effects, all have different degrees of changes. In Fig. 16(d), the image contrast is remarkably enhanced; the details become clearer with brighter color. However, the color tone significantly shifts and loses the true color of the original appearance. Fig. 16(b) and (e) have minimal tone shifting overall; however, the improvement effect is still not ideal, while the homogenous filtering method results in a darker color with a lower contrast in the image. On the contrary, the method proposed in this paper shows obvious improvement to the hazy image in both tone and detail recovery. The visual effect is obviously better than that of the above methods.

Fig. 17 presents five groups of experimental results. Fig. 17(a)–(e) are the original image and the results by He's method [17], Tarel's method [18], Meng's method [36], and the proposed method, respectively. The figures show that all of the above methods have improved the visual effects for hazy images including the contrast. However, for the sky areas in images, both block noise and serious distortion phenomena are seen when using He's method [17] or Meng's method [36]. This is due to the fact that the estimated value of the sky transmission map is too small, thus exaggerating the noise and the color range to a large degree. Although the sky area is smooth after processing by Tarel's method [18], a white edge phenomena occurs at the border between the sky area and the non-sky area in the restored images (e.g., the enlarged part in the rectangle in the fifth image). Since the proposed method in this paper applies a special treatment to the whole image's transmission map using fusion, the contrast between the sky area and the non-sky area in the restored image is high, and there is a natural border transition, so the overall image effect is natural.

4.2. Computational complexity

To verify the advantages of this method in terms of running speed, images of different sizes are used for experiments. The proposed method is compared to He's method [17], Tarel's method [16], and Meng's method [36]. Table 1 shows that He's method [17] has the lowest computing efficiency when processing a single image, mainly because soft matting is a solution problem for large-scale sparse linear systems with high computation complexity and can only compute images of limited sizes. Tarel's method [18] adopts a median filtering for optimization, but as the size of the images increases, the computational complexity also rapidly increases. Meng's method [36] and the proposed method both have almost equivalent computation efficiency, but our algorithm adopts a guide filtering method and has the advantage of a faster running speed when the image is enlarged.

4.3. Results on heavy hazy image

The proposed algorithm is also test on the images with very heavy haze, which is a big challenge work, and the experimental results are shown in Fig. 18. The first line is hazy image and the second line is according haze-free image. It can be seen that the restored images are not satisfied, only the objects with thin haze are recovered as well as the traditional image-restoration methods

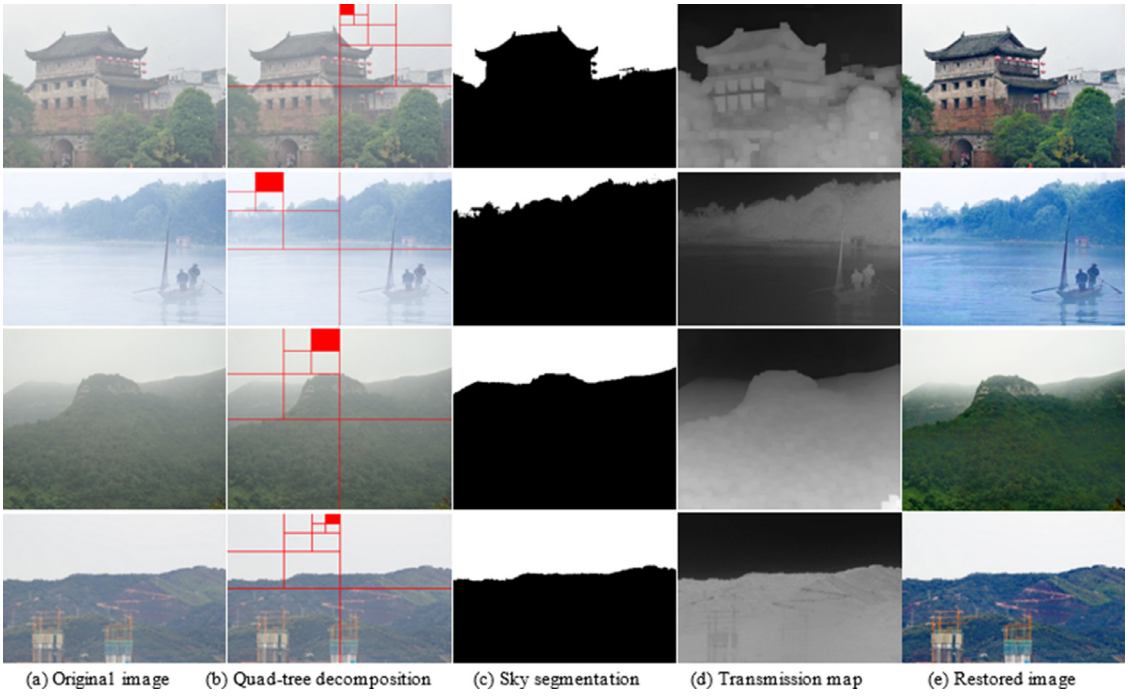

Fig. 15. Dehazing experimental results by proposed method. (For interpretation of the references to color in this figure, the reader is referred to the web version of this article.)

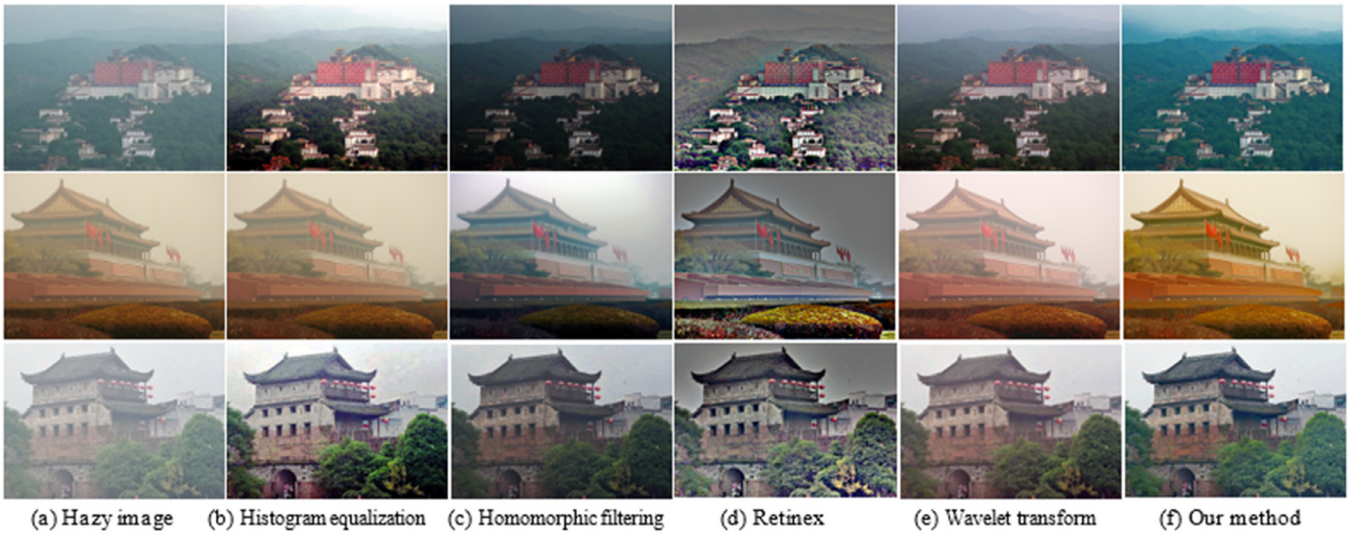

Fig. 16. Comparison between proposed method and traditional image enhancement.

Table 1
Comparison on computational complexity.

Resolution	He's method [17]	Tarel's method (s) [18]	Meng's method (s) [36]	Proposed method (s)
600 × 400	21.76 s	7.65	1.24	1.06
800 × 600	47.92 s	23.14	2.29	1.98
1024 × 768	83.77 s	56.87	3.79	3.77
1600 × 1200	Out of memory	303.15	9.38	7.89

[17,18,36,37]. However, no block effect exists in the restored image, which is in line with the human visual perception.

5.. Conclusions

To address the problems of block effect and color distortion in DCP-based methods, an optimization algorithm is proposed based on region decomposition and features fusion in this paper. In which the sky sub-region is obtained using quad-tree decomposition based on the regional grayscale and gradient information, and it is used to extract seed point for region growing in order to segment the image into sky and non-sky regions. The Gaussian filter is applied for smoothing on the segmented image, and the smoothed image is then used as a weight map to optimize the transmis-

Fig. 17. Experimental results comparison with various methods.

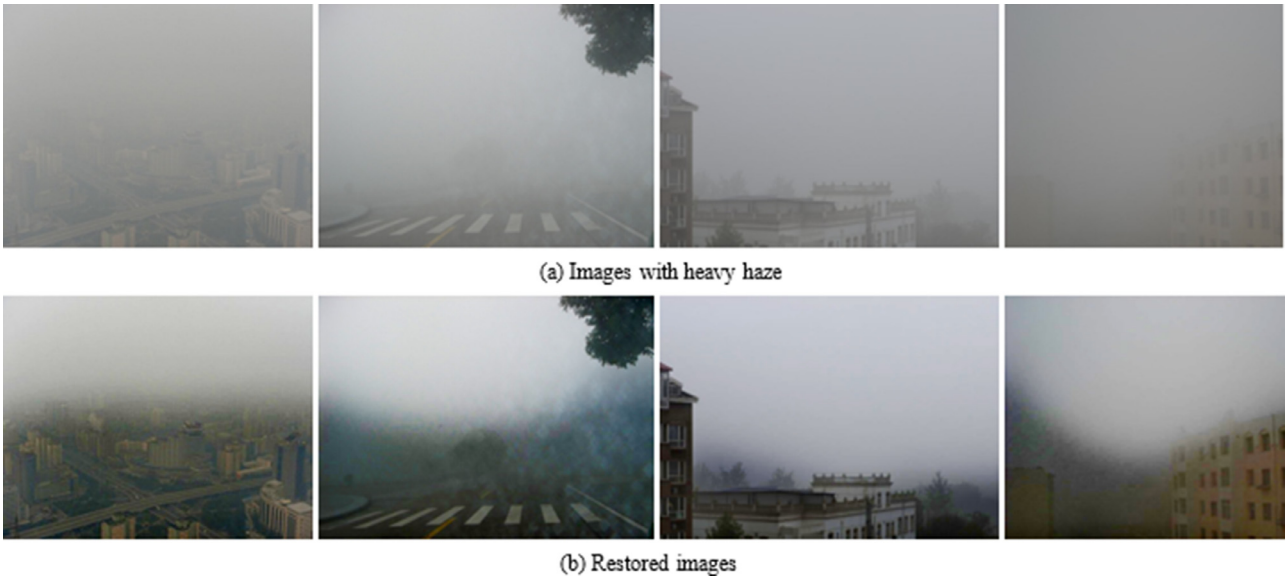

Fig. 18. Experimental results on heavy hazy images.

sion map. In addition, color compensation method is designed to resolve the low brightness problem of restored image based on human visual perception mechanism. Experimental results demonstrated that the images restored using our proposed algorithm are clear and natural, and is particularly well adapted for hazy image processing with large sky areas. The main problem of this algorithm is that the image processing efficiency is still not sufficient for video processing. Thus, further improvements are required to the computational efficiency in the future.

Acknowledgments

This work has been supported by National Natural Science Foundation of China (Grant no. 61403283), Shandong Provincial Natural Science Foundation (nos. ZR2013FQ036 and ZR2015PE025), the Spark Program of China (no. 2013GA740053), the Spark Program of Shandong Province (no. 2013XH06034) and Technology Development Plan of Weifang City (no. 201301015).

Reference

[1] J. Li, H. Zhang, D. Yuan, M. Sun, Single image dehazing using the change of detail prior, Neurocomputing 156 (2015) 1–11.
[2] S.C. Huang, B.H. Chen, Y.J. Cheng, An efficient visibility enhancement algorithm for road scenes captured by intelligent transportation systems, IEEE Trans. Intell. Transp. Syst. 15 (5) (2014) 2321–2332.
[3] B.H. Chen, S.C. Huang, Edge collapse-based dehazing algorithm for visibility restoration in real scenes, J. Disp. Technol. 16 (9) (2016) 964–970.
[4] J. Wang, N. He, L. Zhang, K. Lu, Single image dehazing with a physical model and dark channel prior, Neurocomputing 149 (2015) 718–728.
[5] T.K. Kim, J.K. Paik, B.S. Kang, Contrast enhancement system using spatially adaptive histogram equalization with temporal filtering, IEEE Trans. Consum. Electron. 44 (1) (1998) 82–86.
[6] T.J. Cooper, F.A. Baqai, Analysis and extensions of the Frankle–McCann Retinex algorithm, J. Electron. Imaging 13 (1) (2004) 85–92.
[7] M.J. Seow, V.K. Asari, Ratio rule and homomorphic filter for enhancement of digital colour image, Neurocomputing 69 (7) (2006) 954–958.
[8] S. Dippel, M. Stahl, R. Wiemker, T. Blaffert, Multiscale contrast enhancement for radiographies: Laplacian pyramid versus fast wavelet transform, IEEE Trans. Med. Imaging 21 (4) (2002) 343–353.
[9] J.P. Oakley, B.L. Satherley, Improving image quality in poor visibility conditions using models using model for degradation, IEEE Trans. Image Process. 7 (2) (1988) 167–179.
[10] S.G. Narasimhan, S.K. Nayar, Interactive (de) weathering of an image using physical models, in: Proceedings of the 2003 IEEE International Conference on Computer Vision Workshop on Color and Photometric Methods in Computer Vision, 2003, pp. 1–8.
[11] N. Hautiere, J.P. Tarel, D. Aubert, Towards fog-free in-vehicle vision systems through contrast restoration, in: Proceedings of the 2007 IEEE Conference on Computer Vision and Pattern Recognition, 2007, pp. 1–8.
[12] J. Kopf, B. Neubert, B. Chen, M.F. Cohen, D. Cohen-Or, O. Deussen, M. Uyttendaele, D. Lischinski, Deep photo: model-based photograph enhancement and viewing, ACM Trans. Graph. (TOG) 27 (5) (2008) 116.
[13] Y.Y. Schechner, S.G. Narasimhan, S.K. Nayar, Instant dehazing of images using polarization, in: Proceedings of the 2001 IEEE Conference on Computer Vision and Pattern Recognition, 2001, pp. 325–332.
[14] S.K. Nayar, S.G. Narasimhan, Vision in bad weather, in: Proceedings of the 1999 IEEE International Conference on Computer Vision, 2, 1999, pp. 820–827.
[15] R.T. Tan, Visibility in bad weather from a single image, in: Proceedings of the 2008 IEEE Conference on Computer Vision and Pattern Recognition, 2008, pp. 1–8.
[16] R. Fattal, Single image dehazing, in: Proceedings of the 2008 ACM Transactions on Graphics (TOG), 2008, pp. 1–9.
[17] K. He, J. Sun, X. Tang, Single image haze removal using dark channel prior, IEEE Trans. Pattern Anal. Mach. Intell. 33 (12) (2011) 2341–2353.
[18] J.P. Tarel, N. Hautiere, Fast visibility restoration from a single color or gray level image, in: Proceedings of the 2009 IEEE International Conference on Computer Vision, 2009, pp. 2201–2208.
[19] L. Kratz, K. Nishino, Factorizing scene albedo and depth from a single foggy image, in: Proceedings of the 2009 IEEE International Conference on Computer Vision, 2009, pp. 1701–1708.
[20] J.H. Kim, W.D. Jang, J.Y. Sim, C.S. Kim, Optimized contrast enhancement for real-time image and video dehazing, J. Vis. Commun. Image Represent. 24 (3) (2013) 410–425.
[21] C.O. Ancuti, C. Ancuti, Single image dehazing by multi-scale fusion, IEEE Trans. Image Process. 22 (8) (2013) 3271–3282.
[22] Z. Ma, J. Wen, C. Zhang, Q. Liu, D. Yan, An effective fusion defogging approach for single sea fog image, Neurocomputing 173 (2016) 1257–1267.
[23] Y. Wang, C. Fan, Single image defogging by multiscale depth fusion, IEEE Trans. Image Process. 23 (11) (2014) 4826–4837.
[24] D. Park, D.K. Han, H. Ko, Single image haze removal with WLS-based edge-preserving smoothing filter, in: Proceedings of the 2013 IEEE International Conference on Acoustics, Speech and Signal Processing, 2013, pp. 2469–2473.
[25] J. Yu, C. Xiao, D. Li, Physics-based fast single image fog removal, in: Proceedings of the 2010 IEEE International Conference on Signal Processing, 2010, pp. 1048–1052.
[26] K. He, J. Sun, X. Tang, Guided image filtering, IEEE Trans. Pattern Anal. Mach. Intell. 35 (6) (2013) 1397–1409.
[27] K. Gibson, T. Nguyen, Fast single image fog removal using the adaptive wiener filter, in: Proceedings of the 2013 International Conference on Image Processing, 2013, pp. 714–718.
[28] S.C. Huang, B.H. Chen, W.J. Wang, Visibility restoration of single hazy images captured in real-world weather conditions, IEEE Trans. Circuits Syst. Video Technol. 24 (10) (2014) 1814–1824.
[29] S.C. Huang, J.H. Ye, B.H. Chen, An advanced single-image visibility restoration algorithm for real-world hazy scenes, IEEE Trans. Ind. Electron. 62 (5) (2015) 2962–2972.
[30] K.B. Gibson, D.T. Vo, T.Q. Nguyen, An investigation of dehazing effects on image and video coding, in: Proceedings of the 2012 IEEE Transactions on Image Processing, 21, 2012, pp. 662–673.
[31] B. Xie, F. Guo, Z. Cai, Improved single image dehazing using dark channel prior and multi-scale retinex, in: Proceedings of the 2010 International Conference on Intelligent System Design and Engineering Application (ISDEA), Changsha, China, 2010, pp. 848–851.
[32] B.H. Chen, S.C. Huang, J.H. Ye, Hazy image restoration by bi-histogram modification, ACM Trans. Intell. Syst. Technol. 6 (4) (2015) 1–17.
[33] Z. Li, J. Zheng, Z. Zhu, W. Yao, S. Wu, Weighted guided image filtering, IEEE Trans. Image Process. 24 (1) (2015) 120–129.
[34] J. Jiang, T. Hou, M. Qi, Improved algorithm on image haze removal using dark channel prior, J. Circuits Syst. 16 (2) (2011) 7–12.
[35] J. Shen, On the foundations of vision modeling: I. Weber's law and Weberized TV restoration, Phys. D Nonlinear Phenom. 175 (3) (2003) 241–251.
[36] G. Meng, Y. Wang, J. Duan, S. Xiang, C. Pan, Efficient image dehazing with boundary constraint and contextual regularization, in: Proceedings of the 2003 IEEE International Conference on Computer Vision, 2013, pp. 617–624.
[37] Q. Zhu, J. Mai, L. Shao, A fast single image haze removal algorithm using color attenuation prior, IEEE Trans. Image Process. 24 (11) (2015) 3522–3533.
[38] Z. Li, J. Zheng, Edge-preserving decomposition-based single image haze removal, IEEE Trans. Image Process. 24 (12) (2015) 5432–5441.
[39] W. Ni, X. Gao, Y. Wang, Single satellite image dehazing via linear intensity transformation and local property analysis, Neurocomputing 175 (2016) 25–39 Part A.
[40] W. Wang, X. Yuan, X. Wu, Y. Liu, S. Ghanbarzadeh, An efficient method for image dehazing, in: Proceedings of the 2016 IEEE International Conference on Image Processing, 2016, pp. 2241–2245.

Wencheng Wang received the B.S. degree in automatic engineering in 2002, the M.S. and Ph.D. degrees in pattern recognition and intelligent system from the Shandong University, Jinan, in 2005 and 2011, respectively. And now he is an associate professor of department of information and automatic engineering in Weifang University. From 2006 to 2007, he was visiting scholar at Qingdao University of Science and Technology, and now he is a visiting scholar in University of North Texas and engaging in the research of computer vision and automatic detection technology, especially on image dehazing. His group has published and authored more than 30 papers on academic journals and conference, four book chapters and 5 patents, and more than 30 papers have been indexed by SCI/EI. His main research interests include computer vision, pattern recognition, and intelligent computing. He is currently serving as an associate editor of international journal Transactions of the Institute of Measurement and Control. He was awarded the Young researcher's award of Weifang University in 2010. He is a member of IEEE.

Xiaohui Yuan received B.S. degree in Electrical Engineering from Hefei University of Technology, China in 1996 and Ph.D. degree in Computer Science from Tulane University in 2004. After his graduation, he worked at the National Institutes of Health on medical imaging and analysis till 2006. He joined the University of North Texas (UNT) as an Assistant Professor in 2006 and was promoted to Associate Professor with tenure in 2012. His research interests include computer vision, data mining, machine learning, and artificial intelligence. He served as PI and co-PI in projects supported by Air Force Lab, National Science Foundation (NSF), Texas Advanced Research Program, Oak Ridge Associated Universities, and UNT. His research findings are reported in over 70 peer-reviewed papers. He is a recipient of Ralph E. Powe Junior Faculty Enhancement award in 2008 and the Air Force Summer Faculty Fellowship in 2011, 2012, and 2013. He also received two research awards and a teaching award from UNT in 2007, 2008, and 2012, respectively. He served in the editorial board of several international journals and served as session chairs in many conferences, as well as panel reviewer for funding agencies including NSF, NIH, and Louisiana Board of Regent's Research Competitiveness program. He is a member of IEEE and SPIE.

Xiaojin Wu received the Ph.D. degree in 2011. And now he is working in College of Information and Control Engineering, Weifang University. He has published and authored more than 10 papers on academic journals and conferences. His main research interests include intelligent system and image processing.

Yunlong Liu was born in Rizhao City, Shandong Province, PR China, in 1982. He received his Ph.D. degree in Marine sciences from Ocean University of China in 2012. Since 2012, he has been working as a lecturer in the College of Information and Control Engineering at Weifang University, PR China. He has published and authored more than 20 papers on academic journals and conferences. His research interests include variable structure control, intelligent control, singular systems and information processing.